Entropy **2014**, *16*, 4749-4768; doi:10.3390/e16094749

OPEN ACCESS

entropy

ISSN 1099-4300

www.mdpi.com/journal/entropy

Review

Multicomponent and High Entropy Alloys

Brian Cantor

University of Bradford, Bradford BD7 1DP, UK; E-Mail: vcp@bradford.ac.uk;
Tel.: +44-1274-233012; Fax: +44-1274-233003

Received: 4 February 2014; in revised form: 31 July 2014 / Accepted: 12 August 2014 / Published: 26 August 2014

Abstract: This paper describes some underlying principles of multicomponent and high entropy alloys, and gives some examples of these materials. Different types of multicomponent alloy and different methods of accessing multicomponent phase space are discussed. The alloys were manufactured by conventional and high speed solidification techniques, and their macroscopic, microscopic and nanoscale structures were studied by optical, X-ray and electron microscope methods. They exhibit a variety of amorphous, quasicrystalline, dendritic and eutectic structures.

Keywords: alloying strategy; amorphous alloys; fcc single phase; Gibbs phase rule; high entropy alloys; icosahedral phase; multicomponent alloys; quasicrystals; solid solubility

1. Multicomponent Alloys

1.1. Alloying Strategies

The conventional way of developing a new material is to select the main component based upon some primary property requirement, and to use alloying additions to confer secondary properties. This strategy has led to many successful multicomponent materials with a good balance of engineering properties. Typical examples include high-temperature nickel superalloys and corrosion-resistant stainless steels. In some cases two principal components are used, such as in copper-zinc brasses or alumino-silicate refractories.

Cantor [1] was the first to point out that this kind of conventional alloying strategy leads to an enormous amount of knowledge about materials based on one or sometimes two components, but little or no knowledge about materials containing several main components in approximately equal proportions. Information and understanding about alloys close to the corners and edges of a

multicomponent phase diagram is well developed, with much less known about alloys in the centre of the diagram. This is shown schematically for ternary and quaternary systems in Figure 1. In fact, information about alloys in the centre of the phase diagram is limited for most ternary systems, and virtually non-existent for quaternary and higher order systems.

Figure 1. Schematic ternary and quaternary systems, showing regions of the phase diagram which are relatively well known (green) near the corners, and relatively less well known (white) near the centre [2].

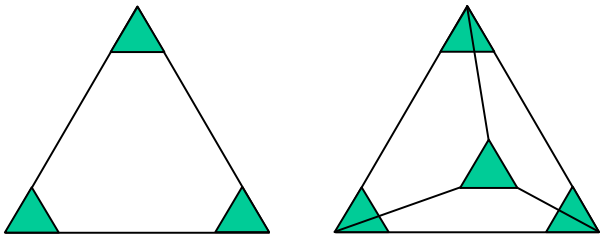

Conventional alloying strategy has been very restrictive in exploring the full range of possible materials, since there are many more compositions at the centre of a phase diagram than at the corners and edges. One method of exploring multicomponent phase space is to extend the conventional method and make more alloying additions in larger quantities [3]. A second method is to use equiatomic substitution, *i.e.*, to begin with a material of interest, and replace individual components with multicomponent equiatomic or near-equiatomic mixtures of chemically similar species [4]. Both these methods have been shown to lead to unusual and interesting new material structures and properties [1,3,4].

1.2. Multicomponent and High Entropy Alloys

The first detailed study of multicomponent alloys consisting of a large number of constituents in equal or near-equal proportions was undertaken in 1981 by Vincent [5] and followed up in 1997 by Knight [6], as reported in 2002 by Cantor [7] at the RQ11 conference in Oxford and then published in 2004 by Cantor *et al.* [1]. Ranganathan [8] discussed similar types of alloys in 2003, describing them as multimaterial cocktails, and Yeh *et al.* [9] did likewise in 2004, describing them as high entropy alloys (see also Yeh *et al.* [10,11]). Recently, there has been a growing number of studies of multicomponent and high entropy alloys, as investigators have realised the potential for discovering new materials with valuable properties in the uncharted phase space in the middle of multicomponent systems.

Yeh *et al.*'s term [9–11] "high entropy alloys" has become accepted to refer to multicomponent alloys consisting of a large number of constituents in equal or near-equal proportions. Multicomponent alloys, however, do not in general exhibit particularly high entropy [12], or even high configurational entropy (Yeh *et al.*'s original concept). They often exhibit a surprisingly small number of phases with wide solubility ranges [2], caused partly by high entropy effects. In fact there are many different kinds of multicomponent alloys, whether or not they have a large number of components in equal or near-equal proportions, depending on their development method (conventional alloying, extended alloying,

equiatomic substitution, *etc.*), constituent species (metallic, non-metallic, semi-metal, compound, *etc.*), manufacturing method (casting, rapid solidification, vapour deposition, co-sputtering, *etc.*), and resulting phase structure and microstructure (single phase solid solution, dendritic, duplex eutectic or peritectic, multiphase, amorphous, *etc.*).

2. Underlying Principles

2.1. Gibbs Phase Rule

The Gibbs phase rule gives the relationship between the number of components c and the number of phases p in a material under equilibrium conditions. At constant pressure (e.g., at atmospheric pressure), the Gibbs phase rule is:

$$p + n = c + 1$$

where n is the number of thermodynamic degrees of freedom in the system. The minimum number of degrees of thermodynamic freedom is $n = 0$, so the maximum number of phases in the alloy under equilibrium conditions p_{max} is:

$$p_{\max} = c + 1$$

For instance, the maximum equilibrium number of phases in a binary system ($c = 2$) is 3, corresponding to a point ($n = 0$) in the phase diagram (e.g., a eutectic or eutectoid point). Such 3-phase equilibrium points rarely exist at a given temperature (e.g., at room temperature), so binary alloys under conditions of room temperature equilibrium almost always consist of 1 or 2 phases. Similarly, the maximum number of phases in a ternary system ($c = 3$) is 4, again corresponding to a point ($n = 0$) in the phase diagram, and ternary alloys under conditions of room temperature equilibrium almost always consist of 1, 2 or 3 phases.

Most materials processing and manufacturing methods operate under conditions far removed from equilibrium, and the maximum number of phases can then be greater than that indicated by the Gibbs phase rule, *i.e.,*:

$$p_{\max} > c + 1$$

This allows high temperature, off-stoichiometric and/or transitionary phases to develop and be retained during non-equilibrium cooling or non-equilibrium segregation of alloying elements. Thus, binary alloys often consist of three or, sometimes, four phases at room temperature, and ternary alloys often consist of four or, sometimes, five phases at room temperature.

As seen in the examples discussed below, the number of phases found in a wide variety of multicomponent alloys is often well below the maximum equilibrium number allowed by the Gibbs phase rule, and even further below the maximum number allowed under non-equilibrium conditions. The reasons for this are not well understood.

2.2. How Many Possible Alloys Are There?

Consider an alloy system containing c components. The number of independent components is $c - 1$. Let different materials be specified to a tolerance of x%, *i.e.*, two alloys are distinct if they differ

by at least x% in at least one component. Each component can take on (100/x) different possible compositions and the total number of different possible alloys N is:

$$N = (100/x)^{c-1}$$

The periodic table contains over 100 different elements which can act as components in an alloy system. Excluding elements which are too radioactive, toxic, rare and/or otherwise difficult to use, a maximum of perhaps $c = 60$ is available to be used as components in realistic materials. Engineering material compositions are typically specified to within at least 0.1%, although a much tighter specification is often needed to prevent variations in properties, so $x \leq 0.1$. The total number of possible alloys N is therefore of the order:

$$N \approx (100/0.1)^{59} = 10^{3\times 59} = 10^{177}$$

which is an enormous number of possible materials. A more restricted alloying range, $c = 40$, and a looser material specification, $x = 1$, gives a more (probably overly) conservative estimate:

$$N \approx (100/1)^{39} = 10^{2\times 39} = 10^{78}$$

which is still an enormous number of materials. For comparison, there are ~10^{66} atoms in the galaxy, and the size of the universe is ~10^{34} nm

2.3. How Many Alloys Have Been Investigated?

All unitary, most binary, and a few ternary and other alloy systems have been studied to some extent. The number of alloys which have been investigated N_I is, therefore:

$$N_I < 60 + 60\times 59\times (100/0.1) + 60\times 59\times 58\times (100/0.1)^2 + small \approx 10^{11}$$

and the proportion of all materials that have been investigated is:

$$N_I / N < 10^{11}/10^{78} = 10^{-67}$$

which is vanishingly small. Putting this result another way, there is a remarkably large number of exciting new materials yet to be discovered.

2.4. How Many Alloys Are Expected to Be Single Phase?

Consider a multicomponent system in which the only single phase regions are the terminal solid solutions based on the elements at the corners of the phase diagram. The number of single phase regions is then equal to the number of components c. This is shown schematically for a ternary system in Figure 2a.

Let the average solubility limit be y%, as also shown in Figure 2a. The total number of different single phase alloys N_S is then:

$$N_S = c(y/x)^{c-1}$$

A scan through one of the well-known compilations of binary phase diagrams [13], analysing (for example) 50 binary Ag alloy systems, shows that at room temperature equilibrium ~10% of the

alloys are single phase, and ~90% are two-phase. On average, therefore, $y \sim 5$. For $c = 60$ and $y = 5$, the total number of single phase alloys is:

$$N_S \approx 60(5/0.1)^{60-1} \approx 10^{102}$$

and the fraction of all alloys which are single phase is:

$$N_S / N = \frac{c(y/x)^{c-1}}{(100/x)^{c-1}} = c(y/100)^{c-1} \approx 60(5/100)^{59} \approx 10^{-75}$$

which is again vanishingly small.

Figure 2. (**a**) Schematic ternary system in which the only single phase regions are the terminal solid solutions, with a solubility limit of y%. (**b**) Increased number of single phase regions (not usually seen in ternary or multicomponent systems)[2].

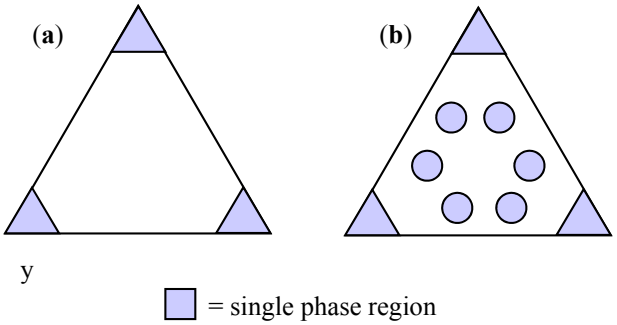

From the above equations, the probability of an alloy being single phase in a multicomponent system is expected to decrease sharply with increasing number of components. As discussed below, however, the number of single phase alloys found in a wide variety of multicomponent alloys is well above the predicted probability. Large numbers of new phases (and crystal structures) are not found in multicomponent alloys, *i.e.*, ternary (and higher order) systems such as shown schematically in Figure 2b are not found experimentally. In other words, the intersolubility between different alloying elements must increase strongly with increasing number of components.

3. Chill Cast and Rapidly Solidified CrMnFeCoNi-NbGeVTiCuMoAlSnZnSiZrNd Alloys

3.1. Chill Cast CrMnFeCoNi-NbGeVTi Alloys

Using equiatomic substitution, Vincent, Knight, Chang and Cantor [1,5,6] investigated the structure of a wide range of chill cast alloys in the CrMnFeCoNiNbGeVTi system. The alloys were based on the generic formula $Cr_xMn_xFe_xCo_xNi_xNb_xGe_xV_xTi_x$. There is a large single phase field of fcc alloys based on the composition $Cr_{20}Mn_{20}Fe_{20}Co_{20}Ni_{20}$ with considerable solubility for the other components. Beyond the boundaries of this single phase field, there is another large two phase field of fcc + bcc alloys. As shown in Table 1, the 5-component $Cr_{20}Mn_{20}Fe_{20}Co_{20}Ni_{20}$ alloy and the 6-component $Cr_{16.7}Mn_{16.7}Fe_{16.7}Co_{16.7}Ni_{16.7}X_{16.7}$ alloys with X=Nb, Cu and V were all single phase fcc, and the 6-component alloys with X=Ge and Ti were two-phase fcc + bcc.

Table 1. Lattice parameters of dendritic fcc and interdendritic bcc phases (nm)[1].

Alloy	fcc	bcc
FeCrMnNiCo	0.359	
FeCrMnNiCoNb	0.362	
FeCrMnNiCoGe	0.358	0.229
FeCrMnNiCoCu	0.359	
FeCrMnNiCoTi	0.364	0.482
FeCrMnNiCoV	0.358	

Figure 3. Scanning electron microscope X-ray maps showing Fe and Cr distributions in an as-solidified cored dendritic structure in chill cast single phase fcc $Cr_{20}Mn_{20}Fe_{20}Co_{20}Ni_{20}$ [2].

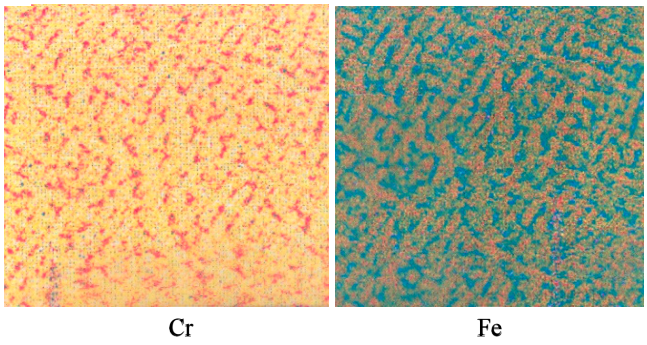

Figure 4. Scanning electron microscope X-ray maps [2] showing Fe and Mn distributions in an as-solidified cored dendritic structure in chill cast single phase fcc $Cr_{20}Mn_{20}Fe_{20}Co_{20}Ni_{2}$.

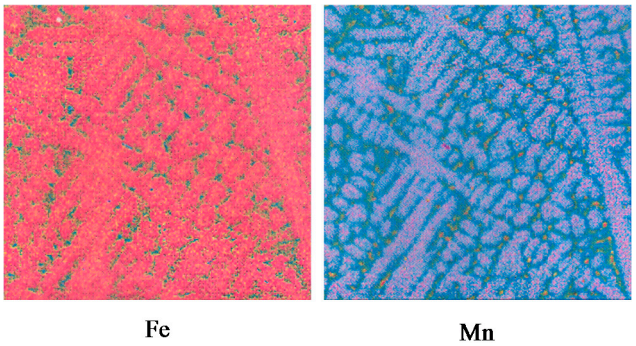

Figure 5. Scanning electron microscope X-ray maps showing Cr, Mn, V and Ti distributions in an as-solidified cored dendritic structure in chill cast $Cr_{14.3}Mn_{14.3}Fe_{14.3}Co_{14.3}Ni_{14.3}V_{14.3}Ti_{14.3}$ [2].

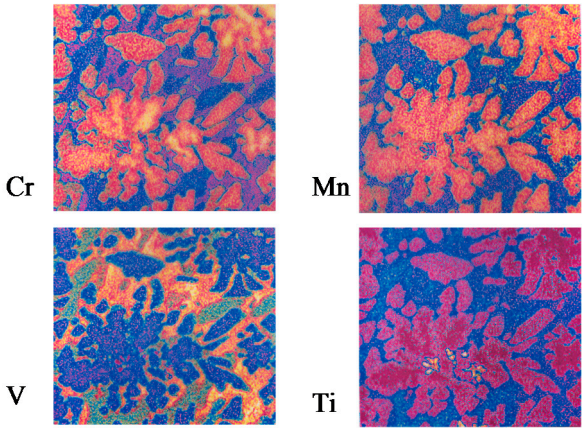

The scanning electron microscope X-ray maps in Figures 3 and 4 show as-solidified cored dendrites in a chill cast single phase fcc 5-component $Cr_{20}Mn_{20}Fe_{20}Co_{20}Ni_{20}$ alloy, with Cr and Fe segregated into the dendrite spines and Mn segregated into the interdendritic spaces. The scanning electron microscope X-ray maps in Figure 5 show as-solidified cored dendrites in a more complex chill cast 7-component $Cr_{14.3}Mn_{14.3}Fe_{14.3}Co_{14.3}Ni_{14.3}V_{14.3}Ti_{14.3}$ alloy, with Cr and Mn segregated in the dendrite spines and V and Ti segregated into the interdendritic spaces.

3.2. Other Modifications to CrMnFeCoNi

A wide range of other multicomponent alloys based on fcc CrMnFeCoNi have been studied. In some cases the single phase fcc structure is altered significantly. For instance, replacing one or other of the components with other transition metals leads to two phase or three phase structures [12]. $Cr_{20}Mn_{20}Fe_{20}Cu_{20}Ni_{20}$, $Mo_{20}Mn_{20}Fe_{20}Co_{20}Ni_{20}$, $Cr_{20}Mn_{20}Fe_{20}Ti_{20}Ni_{20}$, $V_{20}Mn_{20}Fe_{20}Co_{20}Ni_{20}$, and $Cr_{20}Mn_{20}V_{20}Co_{20}Ni_{20}$ consist typically of two phase-separated fcc phases, sometimes with small amounts of topologically close-packed (TCP) intermetallic compound phases such as σ, μ or χ.

However, significant amounts of Al can be added with the single phase fcc structure retained [14,15]. For $x \leq 11$at% in the 5-component system $(Cr_{25}Fe_{25}Co_{25}Ni_{25})_{1-x}Al_x$ the structure is single phase fcc; for $x = 11$–18at%, it is fcc + bcc; and for $x \geq 18$at% it is single phase bcc [14]. Similarly, for $x \leq 8$at% in the 6-component system $(Cr_{20}Mn_{20}Fe_{20}Co_{20}Ni_{20})_{1-x}Al_x$ the structure is single phase fcc; for $x = 8$–16at%, it is fcc + bcc; and for $x \geq 16$at% it is single phase bcc [15]. A single phase fcc structure is retained [16] up to almost $x = 1$at% Sn in $(Fe_{25}Co_{25}Ni_{25}Cu_{25})_{1-x}Sn_x$, but intermetallic compounds are formed at low levels of Mo and Zn additions [17,18]. Replacing Cr and Mn with Cu and Al to form $Cu_{20}Al_{20}Fe_{20}Co_{20}Ni_{20}$ gives a two phase fcc + bcc structure [19], which is retained with additions of Si, Cr or Ti, but is disrupted by the appearance of intermetallic compounds with additions of Zr or Nd.

There has also been considerable study of early transition metal refractory multicomponent single and dual phase bcc alloys [20,21]. A large number of other 5–7 component alloys have been investigated, with a variety of different structures [22,23]. Two conclusions are clear. First, there are large single phase fcc and bcc phase fields in multicomponent transition metal phase space. And secondly, there are usually many fewer phases present than allowed by the equilibrium Gibbs Phase rule.

4. Melt Spun and Chill Cast TiZrHfNbFeCoNiCuAgAl Alloys

Using equiatomic substitution, Kim, Zhang, Warren, Eckert and Cantor [3,24–34] investigated the structure of a wide range of melt spun and chill cast alloys in the TiZrHfNbFeCoNiCuAgAl system. The alloys were based on the generic formula $ETM_{100-x-y}LTM_xAl_y$ where ETM and LTM are early and late transition metals respectively. Typical compositions are $(Ti_{25}Zr_{25}Hf_{25}Nb_{25})_{100-x-y}(Fe_{20}Co_{20}Ni_{20}Cu_{20}Ag_{20})_xAl_y$.

4.1. (Ti,Zr,Hf)-(Ni,Cu)-Al Alloys

A series of $(Ti_{33}Zr_{33}Hf_{33})_{100-x-y}(Ni_{50}Cu_{50})_xAl_y$ glassy alloys were melt spun with compositions in the range $x = 10$–70at% and $y = 10$–30at%. Figure 6 shows typical X-ray diffractograms and Figure 7 shows the resulting ternary phase diagram, containing a large amorphous phase field.

Figure 6. X-ray diffractograms from melt spun amorphous $(Ti_{33}Zr_{33}Hf_{33})_{100-x-y}(Ni_{50}Cu_{50})_xAl_y$ alloys: (**a**) y = 0at%; (**b**) y = 10at%; and (**c**) y = 20at%; and (**d**) y = 30at% [27].

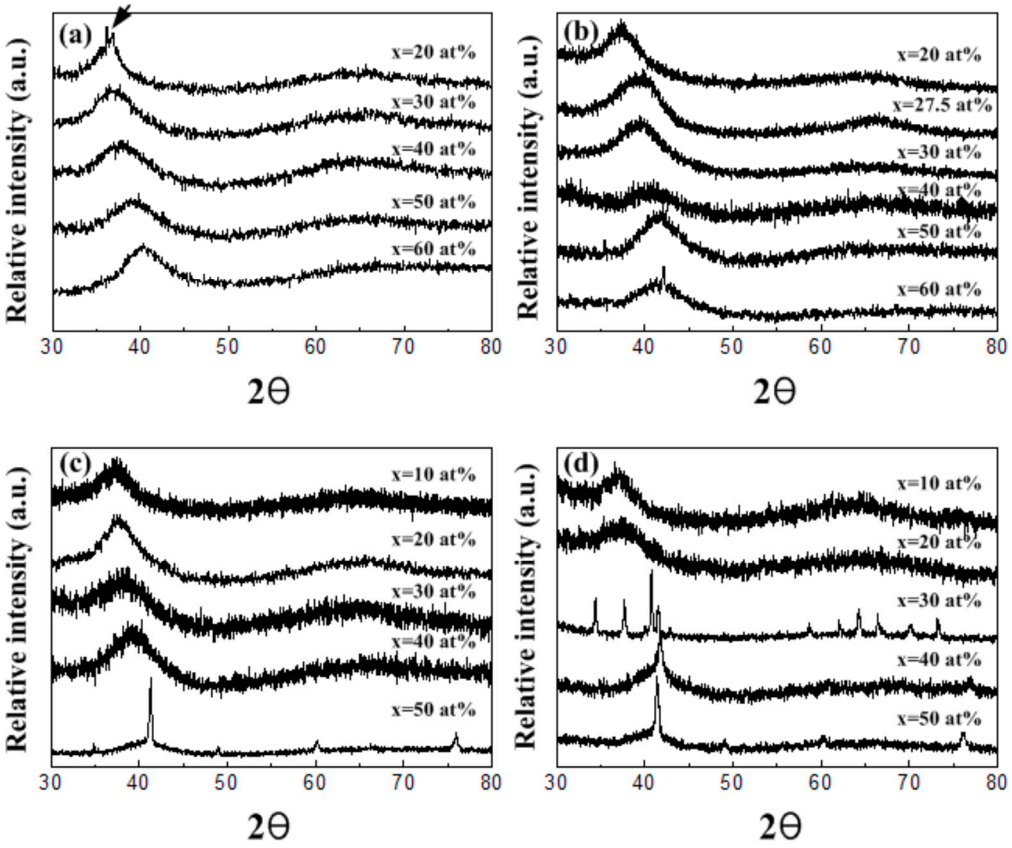

Figure 7. Ternary phase diagram for melt spun $(Ti_{33}Zr_{33}Hf_{33})_{100-x-y}(Ni_{50}Cu_{50})_xAl_y$ alloys, showing a large amorphous phase region [27].

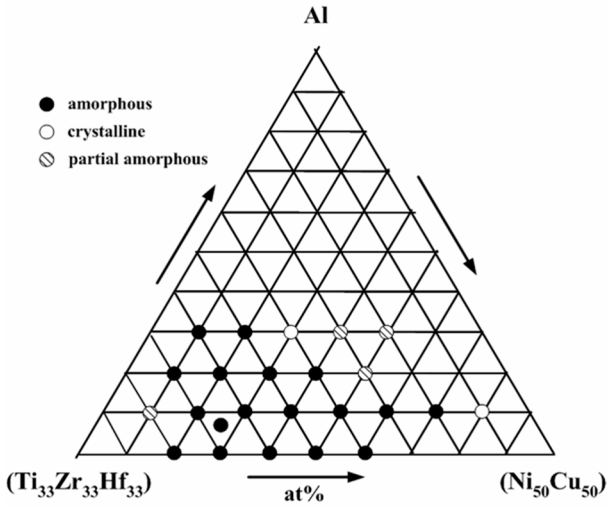

Figure 8 shows typical differential scanning calorimeter traces from different alloys obtained during heating at 20 K/min. The alloys exhibited broad supercooled liquid regions, in the range $\Delta T = T_x - T_g$ = 40–124 K, where T_x = crystallization onset temperature and T_g = glass transition temperature. For $(Ni_{50}Cu_{50})$-rich alloys with x = 50–70at%, crystallization took place with a single exothermic reaction, and for $(Ti_{33}Zr_{33}Hf_{33})$-rich alloys with x = 20–40at%, crystallization took place

with a series of exothermic reactions. Increasing the Al content from y = 10 to 30at% decreased the glass forming ability over a wide range of transition metal compositions x = 40–70at%. The most stable amorphous alloy was $(Ti_{33}Zr_{33}Hf_{33})_{40}(Ni_{50}Cu_{50})_{50}Al_{10}$ with a crystallization temperature of T_x = 818 K. The amorphous alloy with the largest supercooled liquid region was $(Ti_{33}Zr_{33}Hf_{33})_{60}(Ni_{50}Cu_{50})_{20}Al_{20}$ with a crystallization-glass transition temperature difference of $T_x - T_g$ = 124 K.

Figure 8. DSC traces from melt spun amorphous $(Ti_{33}Zr_{33}Hf_{33})_{100-x-y}(Ni_{50}Cu_{50})_xAl_y$ alloys, obtained during heating at 20 K/min: (**a**–**c**) y = 0, 10 and 20at% respectively [27].

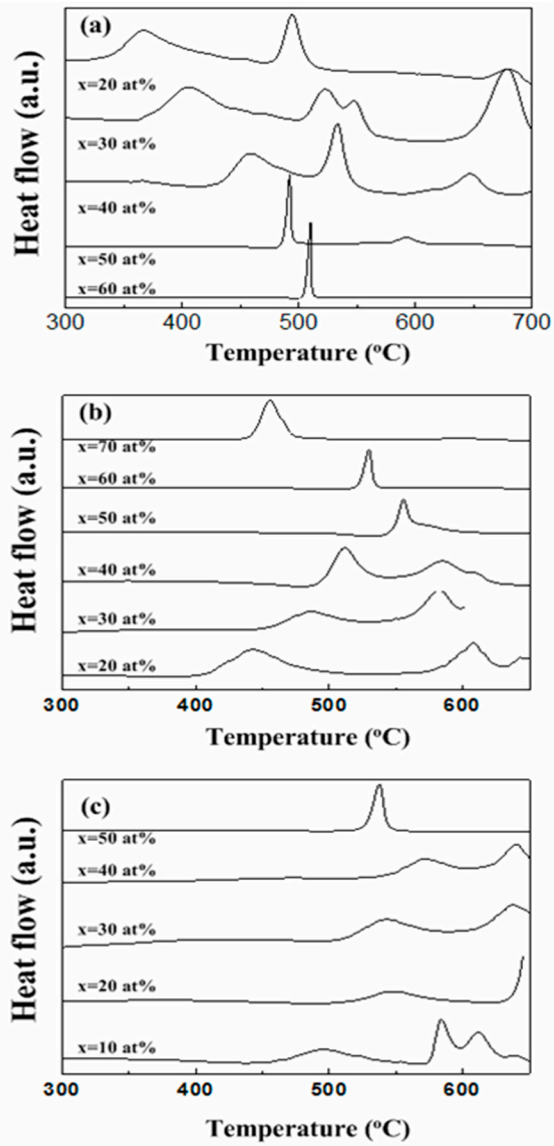

Heat treatment of different alloys showed large single phase icosahedral and Laves phase fields. Figure 9 shows a single Laves phase microstructure in $(Ti_{33}Zr_{33}Hf_{33})_{50}(Ni_{50}Cu_{50})_{40}Al_{10}$ after heat treatment for 1 h at 620 °C, and Figure 10 shows a single icosahedral phase microstructure in $(Ti_{33}Zr_{33}Hf_{33})_{70}(Ni_{50}Cu_{50})_{20}Al_{10}$ after heat treatment for 5 min at 590 °C.

Figure 9. Single Laves phase microstructure in melt spun amorphous $(Ti_{33}Zr_{33}Hf_{33})_{50}(Ni_{50}Cu_{50})_{40}Al_{10}$ after heat treatment for 1 h at 620 °C: (**a**) bright field TEM; (**b**) dark field TEM; and (**c**) selected area diffraction patterns [25].

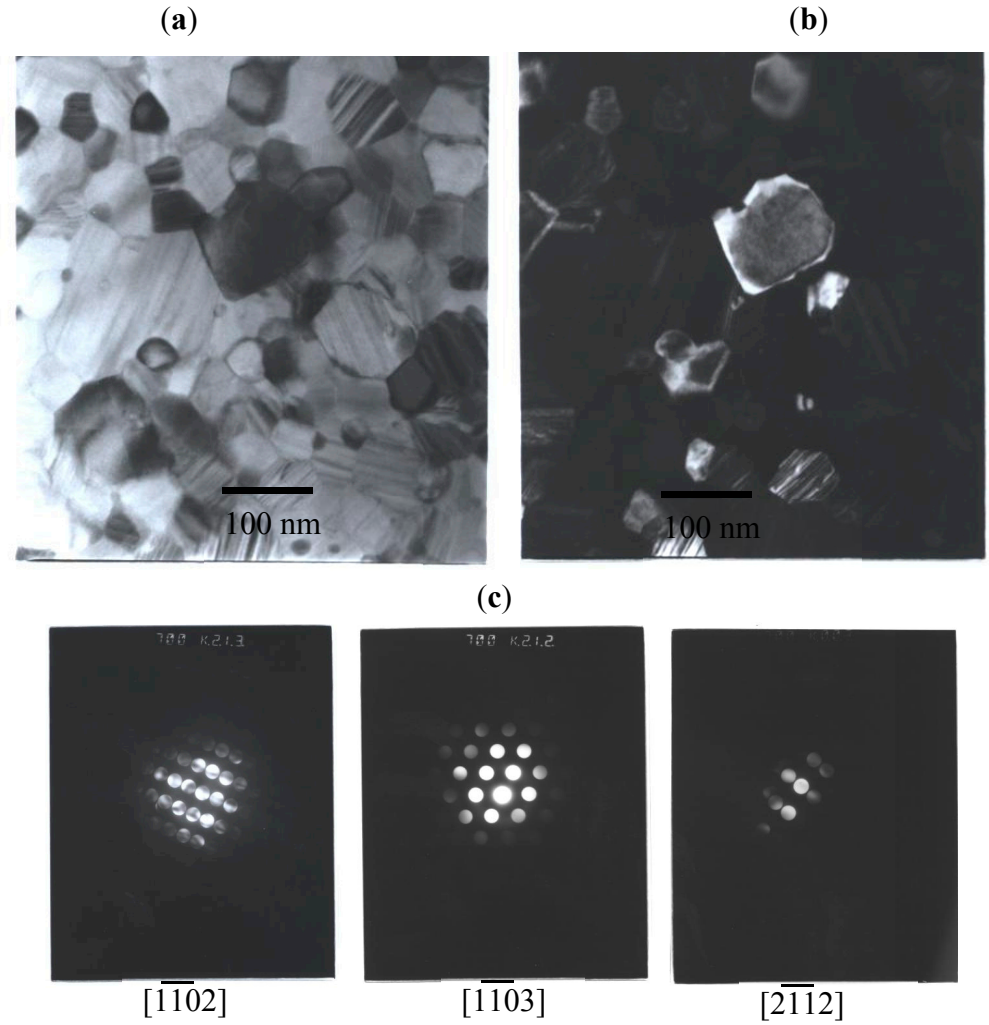

Figure 10. Single icosahedral phase microstructure in melt spun amorphous $(Ti_{33}Zr_{33}Hf_{33})_{70}(Ni_{50}Cu_{50})_{20}Al_{10}$ after heat treatment for 5 min at 590 °C: (**a**) bright field TEM and (**b**–**d**) selected area diffraction patterns [25].

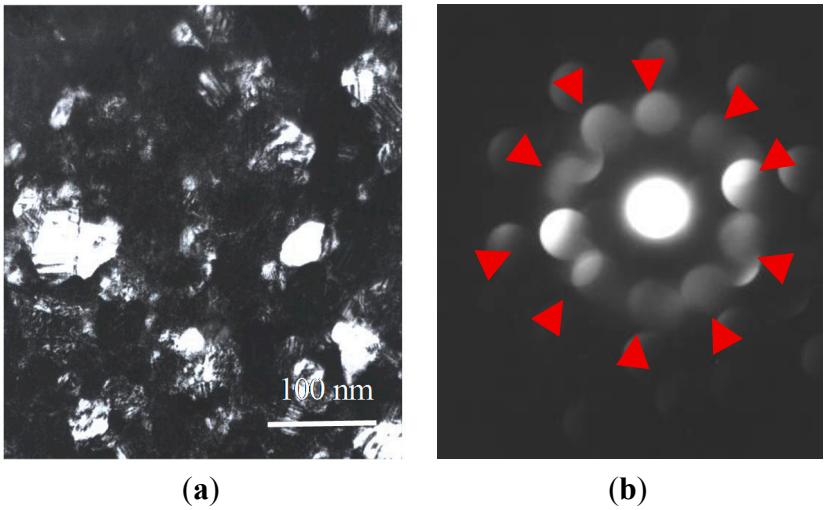

Figure 10. *Cont.*

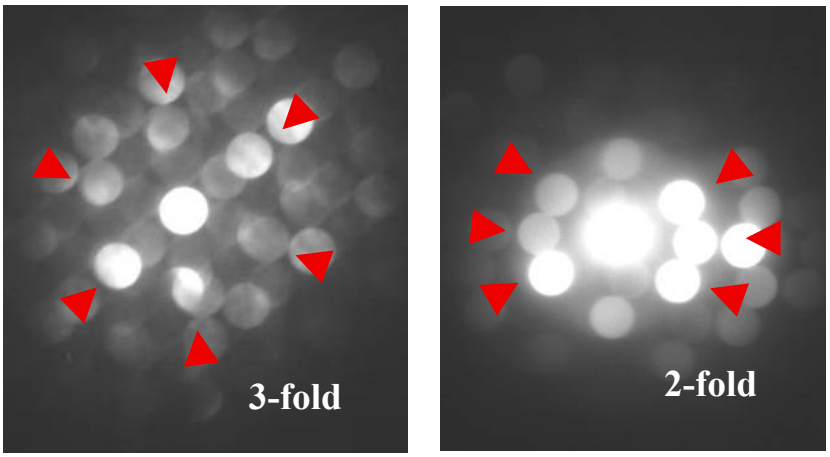

(c) **(d)**

Chill cast $(Ti_{33}Zr_{33}Hf_{33})_{70}(Ni_{50}Cu_{50})_{20}Al_{10}$ forms a mixture of Zr_2Cu-type crystalline, amorphous and icosahedral phases, with micro-scale structural modulations induced by growth strains in the icosahedral matrix, as shown in Figure 11.

Figure 11. Mixture of nanoscale Zr_2Cu-type crystalline, amorphous and icosahedral phases in chill cast $(Ti_{33}Zr_{33}Hf_{33})_{70}(Ni_{50}Cu_{50})_{20}Al_{10}$: (**a**–**c**) bright field TEM; and (**d**–**g**) selected area diffraction patterns [25].

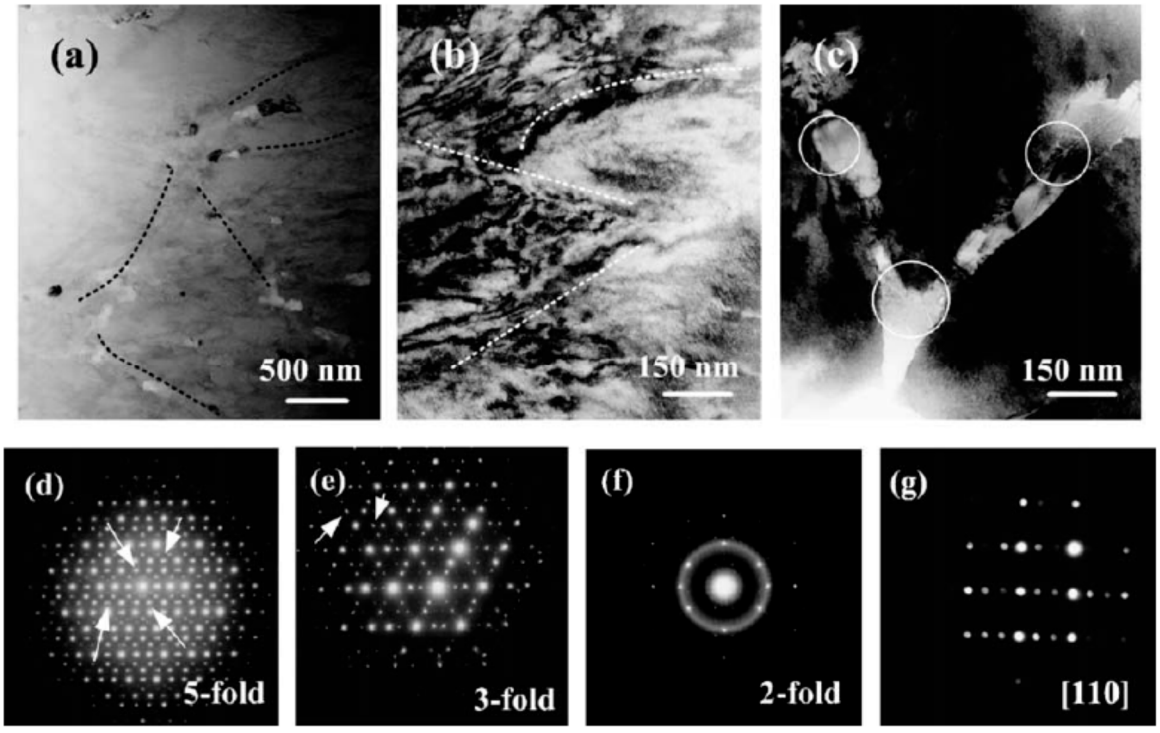

4.2. Melt Spun (Ti,Zr,Hf)-(Fe,Co)-Al Alloys

The effect of using Fe and Co instead of Ni and Cu was studied by melt spinning a series of $(Ti_{33}Zr_{33}Hf_{33})_{90-x}(Fe_{50}Co_{50})_xAl_{10}$ alloys with compositions in the range x = 10–40at%. Only

$(Ti_{33}Zr_{33}Hf_{33})_{70}(Fe_{50}Co_{50})_{20}Al_{10}$ formed a fully amorphous phase in the as-melt spun state, indicating poor glass forming ability. No glass transition temperature was detected in $(Ti_{33}Zr_{33}Hf_{33})_{70}(Fe_{50}Co_{50})_{20}Al_{10}$.

4.3. Melt Spun (Ti,Zr,Hf,Nb)-(Ni,Cu)-Al Alloys

The effect of adding Nb was studied by melt spinning a series of $(Ti_{25}Zr_{25}Hf_{25}Nb_{25})_{90-x}(Ni_{50}Cu_{50})_xAl_{10}$ glassy alloys with compositions in the range x = 10–70at%. Figure 12 shows the resulting X-ray diffractograms and the corresponding ternary phase diagram. The alloys again exhibited broad supercooled liquid regions, in the range ΔT = 35–90 K. Crystallization again took place with a single exothermic reaction for $(Ni_{50}Cu_{50})$-rich alloys with x = 60–70at%, and with a series of exothermic reactions for $(Ti_{25}Zr_{25}Hf_{25}Nb_{25})$-rich alloys with x = 20–50at%. The thermal stability of the amorphous phase was increased by adding Nb.

Figure 12. X-ray diffractograms and corresponding ternary phase diagram from melt spun $(Ti_{25}Zr_{25}Hf_{25}Nb_{25})_{90-x}(Ni_{50}Cu_{50})_xAl_{10}$ alloys [28].

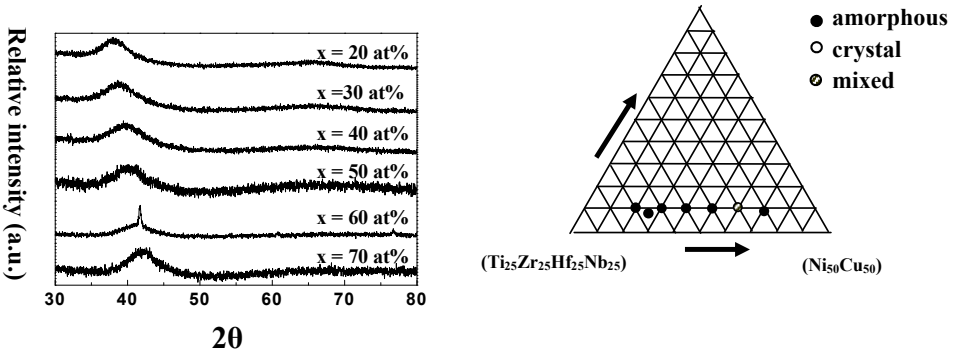

4.4 Melt Spun (Ti,Zr,Hf)-(Ni,Cu,Ag)-Al Alloys

The effect of adding Ag was studied by melt spinning a series of $(Ti_{33}Zr_{33}Hf_{33})_{90-x-y}(Ni_{33}Cu_{33}Ag_{33})_xAl_{10}$ alloys with compositions in the range x = 10–70at%. Figure 13 shows the resulting X-ray diffractograms and the corresponding ternary phase diagram. Compositions in the range x = 20–40 at% again exhibited broad supercooled liquid regions, ΔT = 40–100 K. However, no fully amorphous phase was obtained with compositions in the range x = 50–60at%. Adding Nb and Ag together reduced the amorphous region even further, as shown in Figure 14.

Figure 13. X-ray diffractograms and corresponding ternary phase diagram from melt spun $(Ti_{33}Zr_{33}Hf_{33})_{90-x}(Ni_{33}Cu_{33}Ag_{33})_xAl_{10}$ alloys [28].

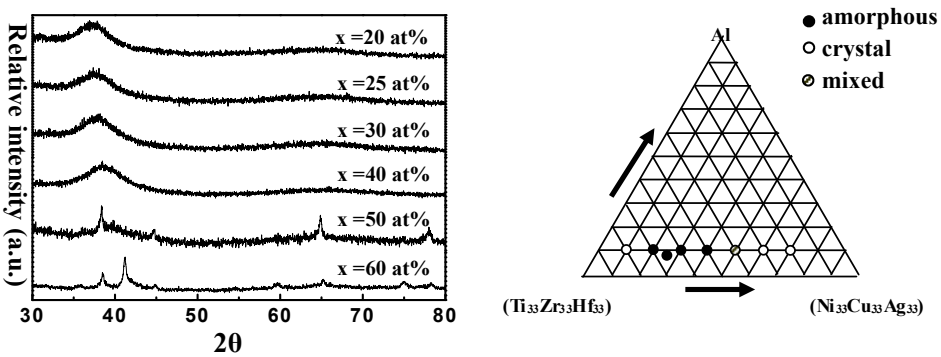

Figure 14. X-ray diffractograms and corresponding ternary phase diagram from melt spun $(Ti_{25}Zr_{25}Hf_{25}Nb_{25})_{90-x}(Ni_{33}Cu_{33}Ag_{33})_xAl_{10}$ alloys [28].

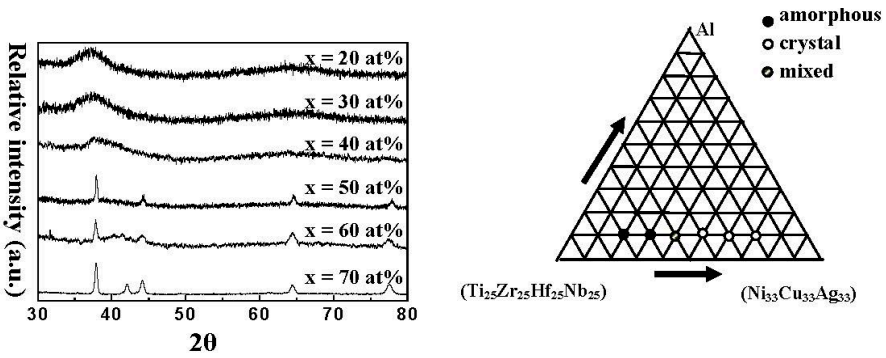

5. Melt Spun AlFeCrTiVNbTa Alloys

5.1. Melt Spun Microstructures

Galano, Audebert, Stone, Prima, Tomut and Cantor [35–45] investigated the structure of a wide range of melt spun alloys in the AlFeCrTiVNbTa system. The alloys were based on the generic formula $Al_{93}Fe_3Cr_2ETM_2$ where ETM is an early transition metal. The as-melt spun alloys consisted mainly of nanoscale icosahedral particles embedded in an fcc Al matrix, as shown in Figures 15 and 16 for (a) $Al_{93}(Fe_3Cr_2)_7$, (b) $Al_{93}Fe_3Cr_2Ti_2$, (c) $Al_{93}Fe_3Cr_2V_2$, (d) $Al_{93}Fe_3Cr_2Nb_2$ and (e) $Al_{93}Fe_3Cr_2Ta_2$. The Ti, V and Ta alloys also contained a few small particles of crystalline intermetallic $Al_{13}Cr_2$, and the Nb alloy contained a small fraction of Al_3Nb. The ternary alloy had the largest icosahedral particle size, ~200 nm, which reduced to 70–100 nm for the Ti, V, Nb and Ta alloys.

Figure 15. X-ray diffractograms from melt-spun $Al_{93}(Fe_3Cr_2)_7$; $Al_{93}Fe_3Cr_2Nb_2$ and $Al_{93}Fe_3Cr_2Ta_2$ alloys [35].

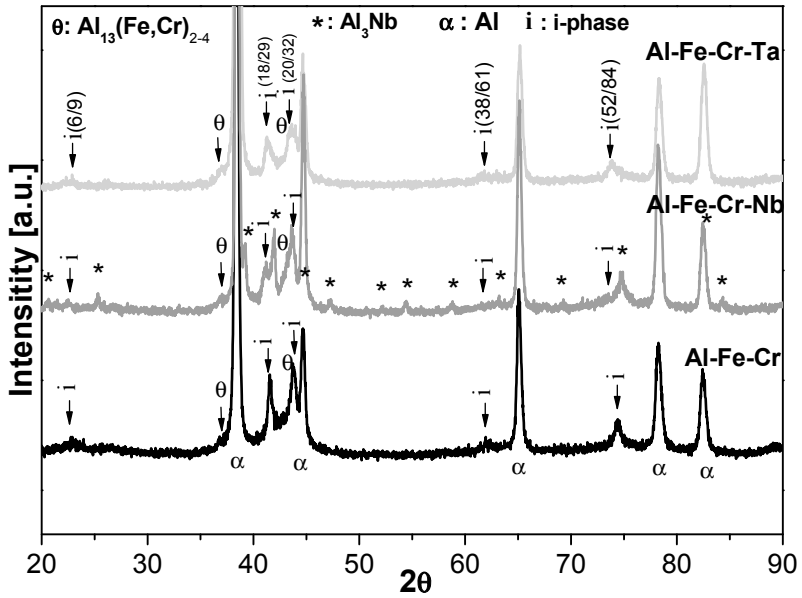

Figure 16. Transmission electron micrographs of icosahedral particles embedded in an fcc Al matrix in melt spun (**a**) $Al_{93}(Fe_3Cr_2)_7$; (**b**) $Al_{93}Fe_3Cr_2Ti_2$; (**c**) $Al_{93}Fe_3Cr_2V_2$; (**d**) $Al_{93}Fe_3Cr_2Nb_2$ and (**e**) $Al_{93}Fe_3Cr_2Ta_2$ alloys [35].

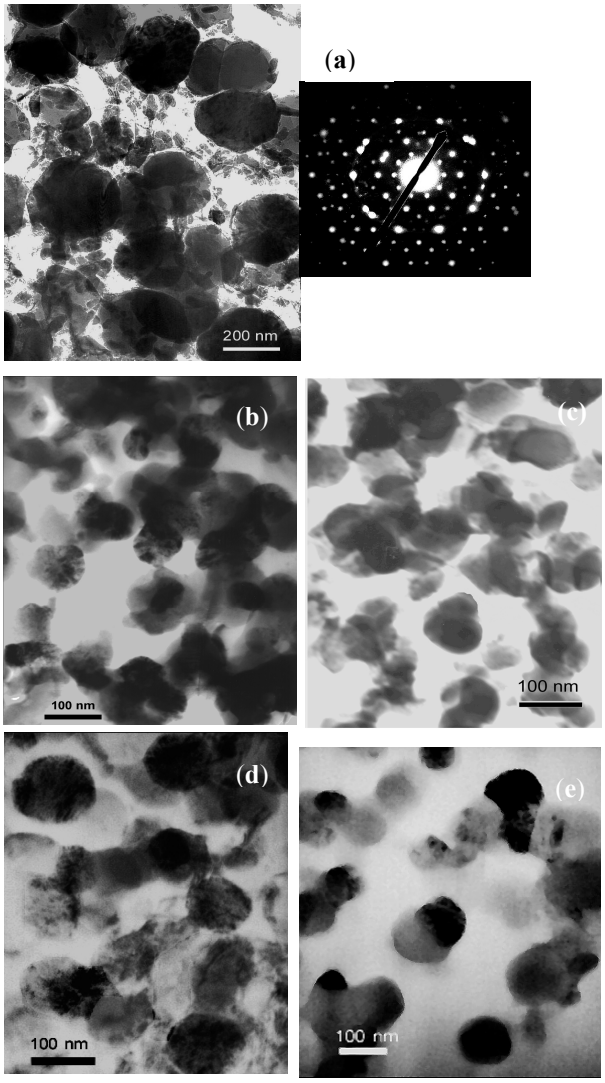

Figure 17 shows a more detailed (a) transmission electron micrograph; (b) selected area electron diffraction pattern and (c) energy dispersive X-ray analysis from an icosahedral particle embedded in melt spun $Al_{93}Fe_3Cr_2Nb_2$. The as-melt spun microstructures were quite stable and resistant to heat treatment, decomposing to form intermetallic particles embedded in an fcc Al matrix after heat treatment at 450–550 °C, as described below.

6.2. Heat Treated Microstructures

The ternary $Al_{93}(Fe_3Cr_2)_7$ alloy microstructure was stable up to 450 °C, when $Al_6(Cr,Fe)$ and $Al_{13}(Cr,Fe)_2$ precipitated. Grain boundary precipitates and small particles inside the Al grains were observed. As shown in Figure 18, the icosahedral particles exhibited rosette shapes and increased in size by about 150%, before decomposing into intermetallic particles after heat treatment at 550 °C.

The $Al_{93}Fe_3Cr_2Ti_2$ alloy microstructure was stable up to 450 °C when small Al_3Ti particles precipitated. The icosahedral particles maintained near-spherical shapes regardless of heat treatment

temperature, but the icosahedral particles formed clusters during heat treatment. Similar clusters were seen in all the alloys. EDX showed that Ti was present in the icosahedral particles as well as in the Al_3Ti precipitates. Icosahedral particles disappeared after heat treatment at 550 °C, and different intermetallic particles appeared with varying morphologies and size.

Figure 17. Icosahedral particle embedded in an fcc Al matrix in melt spun $Al_{93}Fe_3Cr_2Nb_2$: (**a**) transmission electron micrograph; (**b**) electron diffraction pattern; and (**c**) energy dispersive X-ray analysis [37].

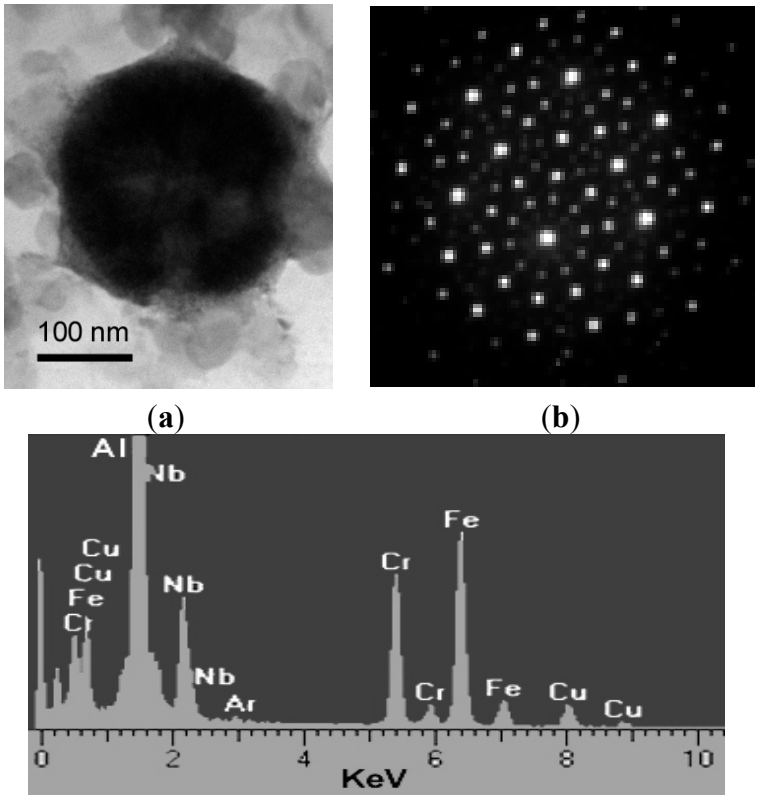

The $Al_{93}Fe_3Cr_2V_2$ alloy microstructure was stable up to 450 °C, when intermetallic particles precipitated. The V alloy showed the highest fraction of intermetallic particles, with V remaining mainly in the icosahedral particles. No icosahedral particles were present after heat treatment at 550 °C.

The $Al_{93}Fe_3Cr_2Nb_2$ alloy microstructure was stable up to 450 °C, when small Al-Nb rich dendrites precipitated. EDX mapping indicated Fe segregation towards icosahedral particle boundaries during heat treatment, as shown in Figure 18. Al-Fe, Al-Cr and Al-Nb rich particles precipitated in the Al grain boundaries, and the icosahedral particle size increased by about 50% with no change in shape. The icoshedral phase was still present after heat treatment at 550 °C.

The $Al_{93}Fe_3Cr_2Ta_2$ alloy microstructure was stable to even higher heat treatment temperatures. No precipitates were seen after heat treatment at 450 °C. The icosahedral particles remained near-spherical, with relatively little increase in size compared with the other alloys, as shown in Figure 18. The icosahedral phase was still present after heat treatment at 550 °C, but disappeared after heat treatment at 600 °C, when different intermetallic precipitates were found.

Figure 18. Bright field STEM images and corresponding EDX maps from: (**a**) $Al_{93}(Fe_3Cr_2)_7$; (**b**) $Al_{93}Fe_3Cr_2Nb_2$; and (**c**) $Al_{93}Fe_3Cr_2Ta_2$ alloys after heat treatment for 30 min at 450 °C [42].

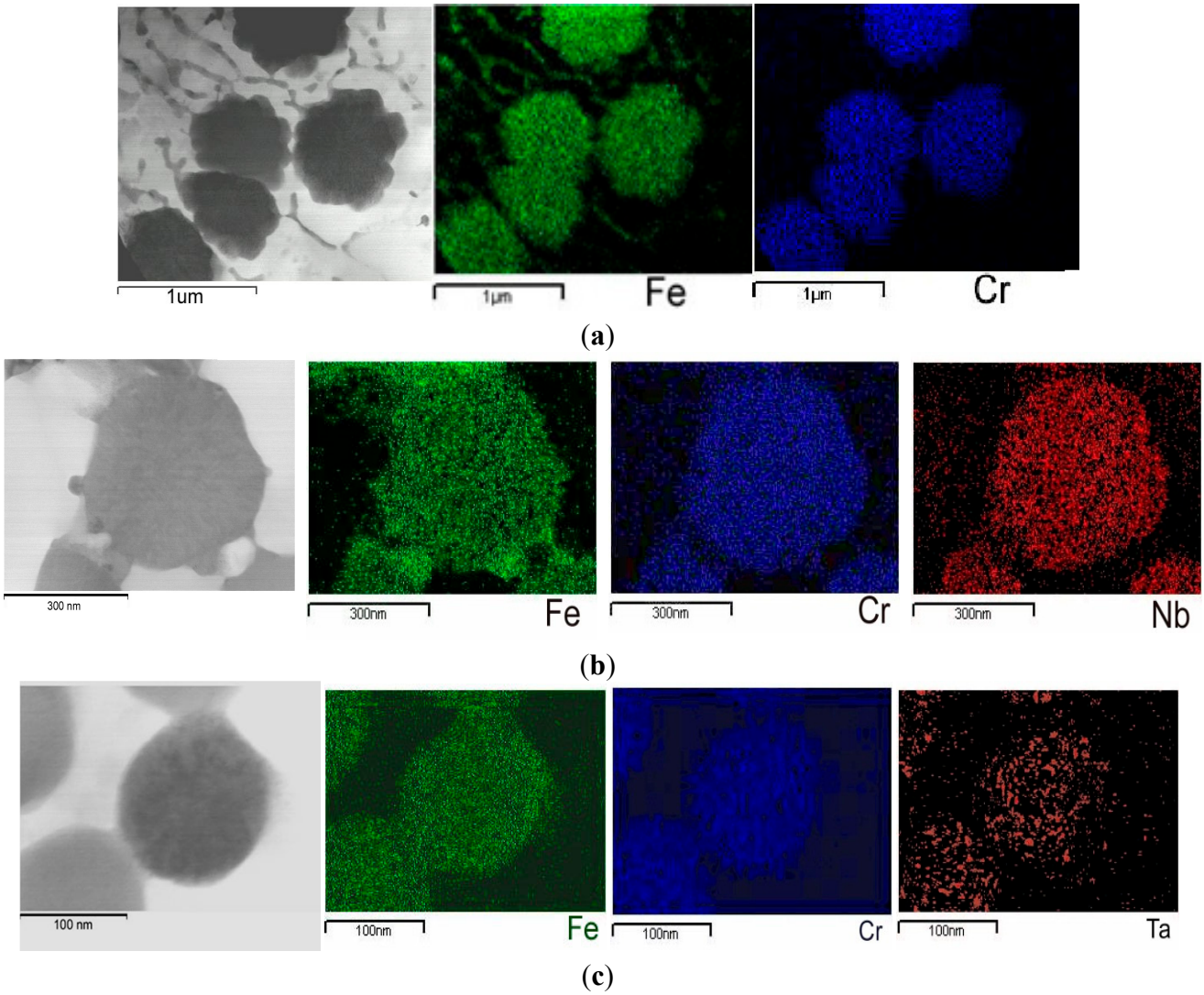

6. Conclusions

A wide range of multicomponent alloys can be manufactured by conventional, extended conventional and equiatomic substitution alloying strategies. The total number of possible materials is enormous, and only a tiny fraction have been manufactured or investigated, almost all close to the corners and edges of the multicomponent phase diagram. Multicomponent alloys show surprisingly few phases, often only one or two and rarely more than three or four, well below the maximum equilibrium number of phases $p_{max} = c + 1$ allowed by the Gibbs phase rule, and even further below the maximum number allowed under non-equilibrium conditions. Similarly, large single phase fields are surprisingly common. These results are associated with increased intersolubility in multicomponent systems and a paucity of new multicomponent compounds.

Chill cast equiatomic substituted CrMnFeCoNiNbGeVTi alloys exhibit single phase fcc and two phase fcc and bcc microstructures. Melt spun equiatomic substituted TiZrHfFeCoNiCuAgAl alloys exhibit fully amorphous microstructures over a wide range of compositions, and often crystallize with

single phase icosahedral and intermetallic crystalline microstructures. Melt spun AlFeCrTiVNbTa alloys consist of icosahedral particles embedded in an fcc α-Al matrix, and are resistant to heat treatment, crystallizing to form intermetallic particles embedded in an fcc α-Al matrix.

Acknowledgments

I would like to thank Isaac Chang, Marina Galano, Ki-Buem Kim, Peter Knight, Francisco Prima, Ian Stone, Marina Tomut, Alain Vincent, Paul Warren and Yuan Zhang for their help in working with me over the years to study multicomponent alloys in my research group at the Department of Materials at the University of Oxford. I would like to thank the Indian Institute of Sciences, Bangalore for the award of a Distinguished Centenary Visiting Professorship, which gave me the time to do much of the work to prepare the manuscript. This review is an extended and updated version of an earlier article [2]. I would particularly like to thank Marina Galano at the University of Oxford and Ki-Buem Kim at Sejong University for supplying some of their recent results, and Kirsty Dales at the University of Bradford for help in preparing the manuscript.

Conflicts of Interest

The authors declare no conflicts of interest.

References

1. Cantor, B.; Chang, I.T.H.; Knight, P.; Vincent, A.J.B. Microstructure development in equiatomic multicomponent alloys. *Mater. Sci. Eng. A* **2004**, *375*, 213–218.
2. Cantor, B. Stable and metastable multicomponent alloys. *Ann. Chim.-Sci. Mater.* **2007**, *32*, 245–256.
3. Inoue, A.; Kimura, H. Bulk amorphous, nanocrystalline and nanoquasicrystalline aluminium alloys. In *Aerospace Materials*; Cantor, B., Assender, H., Grant, P.S., Eds.; IOP Press: London, UK, 2001; Chapter 11, pp. 150–169.
4. Cantor, B.; Kim, K.B.; Warren, P.J. Novel multicomponent amorphous alloys. *Mater. Sci. Forum* **2002**, *386*, 27–32.
5. Vincent, A.J.B. A study of three multicomponent alloys. BSc Part II Thesis, University of Sussex, UK, 1981.
6. Knight, P. Multicomponent alloys. BSc Part II Thesis, University of Oxford, Oxford, UK, 1995.
7. Cantor, B.; Chang, I.T.H.; Knight, P.; Vincent, A.J.B. Microstructure development in equiatomic multicomponent alloys. Presented at Rapidly Quenched and Metastable Materials, Oxford, UK, 25–30 August 2002.
8. Ranganathan, S. Multimaterial cocktails. *Curr. Sci.* **2003**, *85*, 1404.
9. Yeh, J.W.; Chen, S.K.; Lin, S.J.; Gan, J.Y.; Chin, T.S.; Shun, T.T. Nanostructured high entropy alloys with multiple principal elements: Novel alloy design concepts and outcomes. *Adv. Eng. Mater.* **2004**, *6*, 299–303.
10. Yeh, J.W. Recent progress in high entropy alloys. *Ann. Chim.-Sci. Mater.* **2006**, *31*, 633–648.
11. Tsai, K.Y.; Tsai, M.H.; Yeh, J.W. Sluggish diffusion in Co-Cr-Fe-Mn-Ni high entropy alloys. *Acta Mater.* **2013**, *61*, 4887–4897.

12. Otto, F.; Yang, Y.; Bei, H.; George, E.P. Relative effects of enthalpy and entropy on the phase stability of equiatomic high entropy alloys. *Acta Mater.* **2013**, *61*, 2628–2638.
13. Massalski, T.B.; Murray, J.L.; Bennett, L.H.; Baker, H. *Binary Alloy Phase Diagrams*; American Society for Microbiology (ASM): Washington, DC, USA, 1986.
14. Wang, W.R.; Wang, W.L.; Wang, S.C.; Tsai, Y.C.; Lai, C.H.; Yeh, J.W. Effects of Al addition on the microstructure and mechanical properties of $Al_xCoCrFeNi$ high entropy alloys. *Intermetallics* **2012**, *26*, 44–51.
15. He, J.Y.; Liu, W.H.; Wang, H.; Wu, Y.; Liu, X.J.; Nieh, T.G.; Lu, Z.P. Effects of Al addition on structural evolution and tensile properties of the FeCoNiCrMn high entropy alloy system. *Acta Mater.* **2014**, *62*, 105–113.
16. Liu, L.; Zhu, J.B.; Zhang, C.; Liu, J.C.; Jiang, Q. Microstructure and properties of $FeCoCuNiSn_x$ high entropy alloys. *Mater. Sci. Eng. A* **2012**, *548*, 64–68.
17. Shun, T.T.; Chang, L.Y.; Shiu, M.H. Microstructure and mechanical properties of multiprincipal component $CoCrFeNiMo_x$ alloys. *Mater. Charact.* **2012**, *70*, 63–67.
18. Pradeep, K.G.; Wanderka, N.; Choi, P.; Banhart, J.; Murty, B.S.; Raabe, D. Atomic scale characterization of nanocrystalline AlCrCuFeNiZn high entropy alloy using atom probe tomography. *Acta Mater.* **2013**, *61*, 4696–4706.
19. Zhuang, Y.X.; Liu, W.J.; Chen, Z.Y.; Xue, H.D.; He, J.C. Effect of elemental interaction on microstructure and mechanical properties of FeCoNiCuAl alloys. *Mater. Sci. Eng. A* **2012**, *556*, 395–399.
20. Senkov, O.N.; Wilks, G.B.; Miracle, D.B.; Chuang, C.P.; Liaw, P.K. Refractory high entropy alloys. *Intermetallics* **2010**, *18*, 1758–1765.
21. Del Grosso, M.F.; Bozzolo, G.; Mosca, H.O. Modeling of high entropy alloys of refractory elements. *Phys. B* **2012**, *407*, 3285–3287.
22. Yang, X.; Zhang, Y. Prediction of high entropy stabilized solid solution in multicomponent alloys. *Mater. Chem. Phys.* **2012**, *132*, 233–238.
23. Guo, S.; Hu, Q.; Ng, C.; Liu, C.T. More than entropy in high entropy alloys: Forming solid solutions or amorphous phase. *Intermetallics* **2013**, *41*, 96–103.
24. Kim, K.-B. Formation of amorphous and nanocrystalline phases in novel multicomponent alloys. Ph.D Thesis, University of Oxford, Oxford, UK, 2004.
25. Kim, K.-B.; Zhang, Y.; Warren, P.J.; Cantor, B. Crystallization behaviour in a new multicomponent $Ti_{16.6}Zr_{16.6}Hf_{16.6}Ni_{20}Cu_{20}Al_{10}$ metallic glass developed by the equiatomic substitution technique. *Philos. Mag.* **2003**, *83*, 2371–2381.
26. Kim, K.-B.; Warren, P.J.; Cantor, B. Glass forming ability and crystallization behaviour of new multicomponent $(Ti_{33}Zr_{33}Hf_{33})_{60}(Ni_{50}Cu_{50})_{20}Al_{20}$ alloy developed by equiatomic substitution. In *Metastable, Mechnically Alloyed and Nanocrystalline Materials 2002*, Proceedings of the 9th International Symposium on Metastable, Mechanically Alloyed and Nanocrystalline Materials ISMANAM-2002, Seoul, Korea, 8–12 September 2002; Ahn, J.-H., Hahn Y.-D., Eds.; Trans Tech Publications: Zurich-Durnten, Switzerland, 2003; pp. 143–148.
27. Kim, K.-B.; Warren, P.J.; Cantor, B. Formation of metallic glasses in novel $(Ti_{33}Zr_{33}Hf_{33})_{100-x-y}$ $(Ni_{50}Cu_{50})_xAl_y$ Alloys. *Mater. Trans.* **2003**, *44*, 411–413.

28. Kim, K.-B.; Warren, P.J.; Cantor, B. Metallic glass formation in multicomponent (Ti, Zr, Hf, Nb)-(Ni, Cu, Ag)-Al alloys. *J. Non-Cryst. Solids* **2003**, *317*, 17–22.
29. Kim, K.-B.; Warren, P.J.; Cantor, B. Glass-forming ability of novel multicomponent ($Ti_{33}Zr_{33}Hf_{33}$)-($Ni_{50}Cu_{50}$)-Al alloys developed by equiatomic substitution. *Mater. Sci. Eng. A* **2004**, *375*, 317–321.
30. Kim, K.-B.; Warren, P.J.; Cantor, B.; Eckert, J. Crystallization behaviour of Novel $(Ti_{33}Zr_{33}Hf_{33})_{100-x}(Ni_{50}Cu_{50})_x$ alloys with x = 48 to 55. *J. Metastable Nanocryst. Mater.* **2005**, *ISMANAM-2004*, 657–660.
31. Kim, K.-B.; Warren, P.J.; Cantor, B.; Eckert, J. Enhanced thermal stability of the devitrified nanoscale icosahedral phase in novel multicomponent amorphous alloys. *J. Mater. Res.* **2006**, *21*, 823–831.
32. Kim, K.-B.; Warren, P.J.; Cantor, B.; Eckert, J. Structural evolution of nano-scale icosahedral phase in novel multicomponent amorphous alloys. *Philos. Mag.* **2006**, *86*, 281–286.
33. Kim, K.-B.; Warren, P.J.; Cantor, B. Eckert, J. Devitrification of nano-scale icosahedral phase in multicomponent alloys. *Mater. Sci. Eng. A* **2007**, *449*, 983–986.
34. Kim, K.-B.; Warren, P.J.; Cantor, B. Structural relaxation and glass transition behavior of novel $(Ti_{33}Zr_{33}Hf_{33})_{50}(Ni_{50}Cu_{50})_{40}Al_{10}$ alloy developed by equiatomic substitution. *J. Non-Cryst. Solids* **2007**, *353*, 3338–3341.
35. Audebert, F.; Prima, F.; Galano, M.; Tomut, M.; Warren, P.J.; Stone, I.C.; Cantor, B. Structural characterisation and mechanical properties of nanocomposite Al-based alloys. *Mater. Trans.* **2002**, *43*, 2017–2025.
36. Prima, F.; Tomut, M.; Stone, I.C.; Cantor, B. *Nano-Al*; EU TMR Report; European Union: Brussels, Belgium, 2003.
37. Galano, M.; Audebert, F.; Stone, I.C.; Cantor, B. Structural characterisation and stability of new nanoquasicrystalline Al-based alloys. *Mater. Sci. Eng. A* **2004**, *375*, 1206–1211.
38. Prima, F.; Tomut, M.; Stone, I.C.; Cantor, B.; Janickovic, D.; Vlasak, G.; Svec, P. *In situ* resistometric investigation of phase transformations in rapidly solidified Al-based alloys containing dispersed nanoscale particles. *Mater. Sci. Eng. A* **2004**, *375–377*, 772–775.
39. Tomut, M.; Prima, F.; Huenen, G.; Vaughan, G.; Yavari, A.R.; Svec, P.; Stone, I.C.; Cantor, B. Microstructure evolution of high strength AlFeVTi nanoquasicrystalline alloys at elevated temperature. *Mater. Sci. Eng. A* **2004**, *375–377*, 1239–1245.
40. Galano, M. Nanoquasicrystalline alloys. Ph.D Thesis, University of Oxford, Oxford, UK, 2006.
41. Galano, M.; Audebert, F.; Stone, I.C.; Cantor, B. Effect of Nb on nanoquasicrystalline Al-based alloys. *Philos. Mag. Lett.* **2008**, *88*, 269–278.
42. Galano, M.; Audebert, F.; Stone, I.C.; Cantor, B. Nanoquasicrystalline Al-Fe-Cr-based alloys. Part I: Phase transformations. *Acta Mater.* **2009**, *57*, 5107–5119.
43. Galano, M.; Audebert, F.; Escorial, A.G.; Stone, I.C.; Cantor, B. Nanoquasicrystalline Al-Fe-Cr-based alloys. Part II: Mechanical properties. *Acta Mater.* **2009**, *57*, 5120–5130.
44. Galano, M.; Audebert, F.; Escorial, A.G.; Stone, I.C.; Cantor, B. Nanoquasicrystalline Al-Fe-Cr-based alloys with high strength at elevated temperature. *J. Alloys Compd.* **2010**, *495*, 372–376.

45. Audebert, F.; Galano, M.; Saporiti, F. The use of niobium in rapidly solidified aluminium alloys and composites. *J. Alloys Compd.* **2014**, to be published.